

Digital Communication Techniques in Macroscopic Air-Based Molecular Communication

Sunasheer Bhattacharjee, Martin Damrath, Lukas Stratmann,
Peter Adam Hoher, *Fellow, IEEE*, and Falko Dressler, *Fellow, IEEE*

Abstract—An air-based macroscopic molecular communication testbed exploiting fluorescence properties of water-based solutions of Uranine and Rhodamine 6G dyes is presented in this work. The testbed comprises of an industrial sprayer as its transmitter, a 2 m long tube as the transmission channel, and a high-speed camera-based detector. The considered transmission distances cover a range over several tens of centimeters to meters. The analytical end-to-end system model is extended to include the noise model in this work. Various modulation schemes exploiting the concentration levels of the sprayed dyes as the information source have been implemented and their performances are compared to the standard on-off keying. Spatial domain, along with the concentration of the dyes has been introduced as an additional degree of freedom into the testbed to improve the bit rate, and the performance is compared with respect to those modulation schemes using color and concentration levels of the dyes as degrees of freedom. Various equalization techniques and detection algorithms have also been implemented and compared. All comparative analyses are performed with respect to the measurements obtained from the testbed, the analytical models, and the particle-based Pogona simulator.

Index Terms—Molecular communication, end-to-end system model, digital modulation, equalizers, fluorescence, optical detectors, testbed design.

I. INTRODUCTION

MOLECULAR communication (MC) is an emerging interdisciplinary research topic, where particles (in the form of molecules, atoms, or ions) act as information carriers between a transmitter (Tx) and a receiver (Rx), or between several Tx and/or Rx [1]–[5]. MC is inspired by nature in its various forms. For example, social insects such as ants use pheromone-based chemical signaling techniques for communication purposes [6]. Inter- and intra-cellular signaling occurring within the body of a living organism is another example [7], [8]. MC can be applied at micro scale and at macro scale, respectively. Potential micro-scale applications of MC involve sensing of target substances in biotechnology

Reported research was supported by the project *MAMOKO* funded by the German Federal Ministry of Education and Research (BMBF) under grant numbers 16KIS0915 and 16KIS0917. The authors would also like to extend their gratitude to Dr. Fatih Gulec for his invaluable inputs.

S. Bhattacharjee, M. Damrath, and P.A. Hoher are with the Faculty of Engineering, Kiel University, Kiel, Germany, e-mail: {sub,md,ph}@tf.uni-kiel.de.

L. Stratmann and F. Dressler are with the School of Electrical Engineering and Computer Science, TU Berlin, Berlin, Germany, e-mail: {stratmann,dressler}@ccs-labs.org.

Manuscript received November 24, 2021, revised June 07, 2022, accepted October 10, 2022.

and smart drug delivery in medicine [9]. Regarding the macro scale, MC is foreseen to evolve as a feasible alternative targeting those applications, where deployment of infrastructure using traditional wired and wireless communications proves to be challenging. Examples include monitoring underwater environments with high concentration of salt, underground communications, and tunnels as well as terrestrial pipeline networks for detection of leakages [3], [10], [11]. In recent times, prompted by the outbreak of the ongoing pandemic of the *severe acute respiratory syndrome coronavirus 2* (SARS-CoV-2), many works also tried to bridge the gap between macro-scale MC and infectiology in order to find the solutions to minimize the infection rate [12]–[15].

Any industry-specific MC system application, prior to its standardization, would require a framework to encompass various aspects of communication theory such as the channel impulse response (CIR) analysis and channel modeling, high data rate achieving modulation schemes, efficient detection algorithms to achieve lower bit error rate (BER), channel coding techniques for effective error detection and correction, etc. This work aims at achieving some of these goals by performing preliminary tests and analyses in a testbed and simultaneously emulating the behaviors in a simulation environment. This brings more flexibility into the system in terms of seamless addition/alteration of certain parameters, making the study more efficient and holistic.

The first testbed concerning air-based macro-scale MC was introduced in [16], where alcohol was used as the information carrier between Tx (electronic sprayer) and Rx (metal-oxide alcohol sensor). Nonlinearities, high inter-symbol interference (ISI), and saturation level attained by the detector proved to be the major performance deterrents to the system. Other alternatives to alcohol-based MC were thereafter explored (a comprehensive overview of existing testbeds is given in [17]). Among others, detection of odors using volatile organic compounds and a mass spectrometer was presented in [18], considering a distance of 3 m. In this work, the emphasis was laid on a CIR analysis, rather than improving data transmission rates. Transfer of information using a system of chemical vapor emitter and photoionization detectors under a constant gas flow in an enclosed environment was shown in [19], where a bit rate of 20 bit/s was achieved at a BER of 10^{-3} over a distance of 1.4 m. The use of fluorescent dye as an information carrier was initially presented in [20] for a fluid-based channel, employing a particle image velocimetry detection process. The impulse response was much wider in time-domain compared to MC testbeds using air-based channels due to a higher

viscosity, limiting the achievable bit rate. Another MC testbed introducing planar laser-induced fluorescence for signal propagation in a fluid-based environment was presented in [21], where the channel model was based on the detection of the fluorescent dye concentration. The impulse response again, in this case, was much wider in time-domain, lowering the data transmission rates with increased ISI.

A proof of concept for air-based MC using fluorescent dye was presented in [22] over a distance of 50 cm, where a bit rate of 20 bit/s was achieved for on-off keying (OOK). This work was extended in [23] to implement modulation schemes such as molecular shift keying (MoSK) [24] and molecular concentration shift keying (MCSK) [25] using multiple dyes with a detailed BER performance comparison. A bit rate up to 40 bit/s was achieved over a distance of about 2 m at a BER of approximately 10^{-2} for 4-MCSK, while a BER of approximately 10^{-3} was obtained for 2-MoSK for the same amount of distance at a bit rate of 20 bit/s. Similarly, the work presented in [26] used multiple chemicals with unique mass-to-charge ratios to simultaneously transmit information with the help of three new modulation methods, suited to exploit this property. Depending on the environment and the modulation scheme, a transmission distance of up to 4 m was achieved, albeit at much lower data transmission rates in the order of bit/min.

Simulating the testbed in existing simulators for MC faces several issues [30]. Particle-based MC simulators like BiNS2 [31] and AcCoRD [32] as well as analytical simulators like nanoNS3 [33], simulate diffusion of the particles and a typically simplified flow of the surrounding medium, causing the carrier particles to move between Tx and Rx. In the presented testbed, however, the movement of the particles is caused by the sprayer itself. While previous simulators release particles without adding to their velocity, the presented simulator sprays them into the environment with an initial velocity for each particle. The presented nozzle model is calibrated with data from the real testbed for matching opening angle and velocity distributions, following a similar approach in [34]. On the Rx side, the aforementioned simulators count the number of particles within a given region or passing a given section. This approach does not take the perspective of the camera Rx or overlaps of the particles into account (droplets in the foreground obscuring other droplets), that affect the Rx video footage. New models for a spray nozzle and a camera Rx are integrated into the Pogona simulator [35].¹

The main motivation behind this work is to achieve higher transmission distances and bit rates at reasonably small BER. Towards this goal, this work attempts to explore various digital communication techniques (i.e., modulation schemes and equalization) and apply them to the macroscopic air-based MC testbed using fluorescein. Earlier works related to the testbed, mostly dealt with experimental investigations of modulation techniques. In this paper, we extend our previous works to include more modulation schemes as well as equalization techniques to present a holistic investigation by comparing the

testbed measurement results with their respective analytical end-to-end system models and Pogona simulator results. The analytical model and the Pogona simulator give a mathematical description and simulation alternative for estimating the testbed measurements effectively, without needing any bulky physical resources. The main contributions of this paper can be summarized as follows:

- The analytical end-to-end system model of the MC testbed [36] using fluorescent dyes is presented, featuring a noise model that takes into account the correlative behavior between the consecutive noise samples in a signal observed from the testbed measurements.
- Implementation and a detailed comparison of achievable data rates, and BER performances of various modulation schemes with higher degrees of freedom using different dye colors as well as the spatial domain (inspired from [27]–[29]) are presented. For the first time, a resource requirement analysis is shown for the implemented modulation schemes in MC testbed, which could serve as an additional performance metric. Furthermore, the measurement results obtained from the testbed, the analytical model, and the Pogona simulator feature jointly in this particular work.
- Additionally for the first time, a comparison of performances of various detection algorithms with equalization techniques, commonly used in digital communication is applied to the testbed measurements, the analytical model, and the Pogona simulator results.

The remainder of this paper is structured as follows: Section II describes the complete layout of the testbed with each of its components and the implementation in the Pogona simulator. Section III describes the analytical end-to-end system model with the inclusion of the noise model. In Section IV, the various implemented modulation schemes are discussed in detail, with their respective achievable data rates and resource requirements. Section V discusses the detection process and employed algorithms. In Section VI, a BER performance comparison of the implemented modulation schemes and detection algorithms with variation in distance is shown. Finally, this paper is concluded in Section VII with a future outlook.

II. TESTBED AND SIMULATOR REALIZATION

The physical testbed is shown in Fig. 1 consisting of the Tx in the form of a sprayer, the transmission channel, and the camera-based Rx. The water-based dye solution, which is the information carrier, is emitted by Tx in the form of droplets. At Rx side, these droplets get illuminated by an ultra-violet (UV-A) light source, which is captured by the camera as shown in Fig. 2. This section describes the testbed components in detail while outlining the approach used to model them in a particle-based simulator.

A. Information Carriers

The Tx consists of either one or two sprayers containing water-based solutions of Uranine and/or Rhodamine 6G, depending on the implementation of the modulation schemes.

¹<https://www2.tkn.tu-berlin.de/software/pogona/>

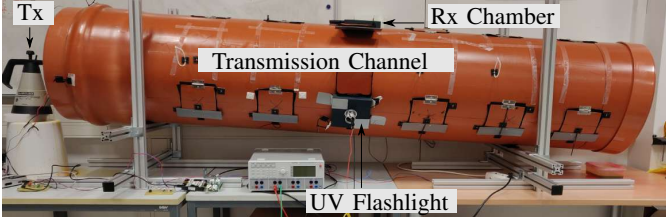


Fig. 1: Testbed for air-based MC using fluorescent dyes via a 2 m long transmission channel.

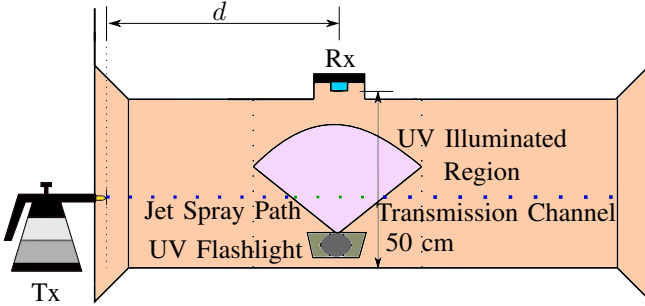


Fig. 2: Air-based MC testbed layout.

Uranine is a disodium salt of fluorescein which is a red amorphous organic compound. Rhodamine 6G on the other hand is a dark reddish-purple crystalline solid organic compound. Both the compounds are slightly soluble in water and alcohol. When excited by a UV-A light source at approximately 398 nm, a Uranine-water-based solution produces a peak emission at approximately 548 nm, while a Rhodamine 6G-water-based solution produces a peak emission at about 585 nm. The emission spectra are presented in Fig. 3. The dye properties do not change when performing the measurements and, therefore, are used reliably to represent the information symbols.

In the simulation scenario, particles represent these information carriers, a common practice to simulate fluids [37]. With the help of the particle positions, it is possible to represent them as spheres in space. Instead of the handling of light sources and the reflection behavior of the particles, each of the visualized spheres has the same uniform color. So, the potential inhomogeneous influences of the light source in the simulation environment are ignored. The size of the particles is also set to an approximately constant value. These simplifications in the simulation environment however, lead to less background noise and uncertainty as compared to a practical scenario, when measuring the end-to-end system impulse response (SIR).

B. Transmitter

The *Gloria Type 89* industrial sprayer is used for spraying the dye solutions and forms the Tx part of the testbed. The maximum capacity of the container is 1 L while the integrated pump generates a pressure up to 3 bar. The liquid is released outside the container through a conical nozzle in either “cloudy” or “jet”-like spray formation. In this work, we consider the “jet” spray form. At a maximum pressure, the spraying volume rate is around 0.54 L/min. The switching

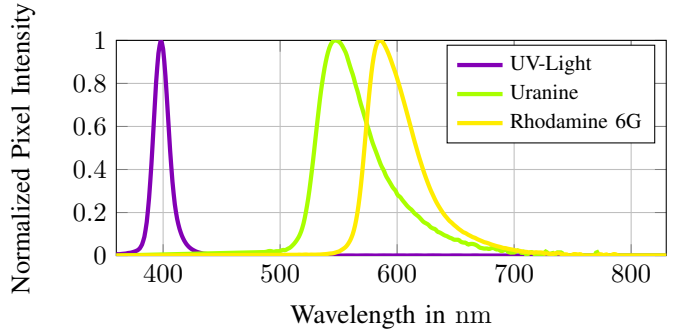


Fig. 3: Spectra of UV-A light source and fluorescent dyes.

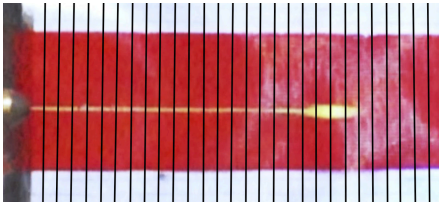
mechanism of the sprayer is electronically controlled by a 12 V solenoid valve placed before the nozzle. The valve has a maximum tolerance pressure of 10 bar which is controlled by a waveform generator and a control circuit. The minimum shutting time of the valve is 30 ms, which influences the shape of the impulse response in the time-domain. The transmitter side can easily be extended to accommodate multiple sprayers with separate water-based dye solutions depending on the modulation schemes used for data transmission.

The presented approach to model this nozzle in a particle-based simulator follows a three parameter model which describes the nozzle by the number of injected particles N , their initial velocity v_{init} , and distribution \mathcal{P} in 2-dimensional space corresponding to the opening angle of the nozzle. When spraying towards a sheet of paper vertically as in Fig. 4b, the shape approximates a circle. Therefore, it is feasible to consider a 2-dimensional model and apply a rotation around the nozzle’s spray direction with a uniformly distributed angle $\alpha \sim \mathcal{U}(0, 2\pi)$ to enable the translation into a 3-dimensional model. It is not possible to measure a clear diameter of the projected circle as it has no hard outline but fades to surrounding droplets. This motivates using a non-uniform distribution for \mathcal{P} for the nozzle model. Each injected particle will have a velocity computed as

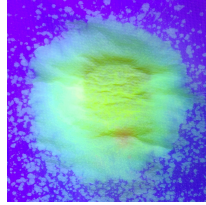
$$\begin{pmatrix} v_x \\ v_y \\ v_z \end{pmatrix} = v_{\text{init}} \cdot \begin{pmatrix} \sin(\beta) \cdot \sin(\alpha) \\ \cos(\beta) \\ \sin(\beta) \cdot \cos(\alpha) \end{pmatrix}, \quad (1)$$

where $\beta \sim \mathcal{P}$. This sprays particles into the positive y -direction. Other spray directions can be realized by performing another rotational transformation on the velocity vectors.

In order to calibrate this model to the spray nozzle used in the testbed, the parameters v_{init} and the distribution \mathcal{P} have to be determined. To estimate the velocity v_{init} and to better understand the spraying process of the nozzle in general, a high-speed camera capturing 1000 frames per second (FPS) provides helpful video footage. A grid paper in the background supports the velocity estimation for the first 30 cm. As the paper is put behind the nozzle with as little distance as possible between nozzle and paper, the perspective offsets can be neglected. The footage outlines a water jet shape which is not affected by air drag as much as a single particle. By tracking the front of the water jet on the grid for each frame, an



(a) Video footage analysis for estimating the velocity of the particles.



(b) Projection of a spray injection on a paper at 117 cm.

Fig. 4: Experiments to obtain a better understanding of the spray nozzle behavior.

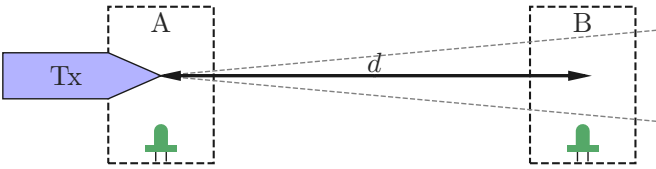


Fig. 5: Setup of an experiment to estimate the speed of the particles by utilizing LEDs to measure the time between transmission start and reception at a given distance.

estimation of the velocity is possible. The water jet speeds up in the first ten frames and reaches a constant velocity for the last frames. The image in Fig. 4a depicts one such frame when the water jet already achieves a constant velocity. Based on ten repetitions of this experiment, a mean velocity of around 12.82 m/s is obtained. Because of the image being blurry, the precision for estimating the head position of the water jet is half the distance between two lines (0.25 cm).

To verify that air drag is negligible even for larger distances in the testbed, the camera footage of the previous experiment would not deliver the required precision for tracking the head of the water jet. Instead, the time between transmission and reception for a known distance d is measured. One camera (A) observes the Tx and an additional LED which is put into the frame (A). The Rx, being a camera as well, has another LED within its view (B). For this experiment, the frame rate of the camera is chosen to be 480 FPS. This setup is outlined in Fig. 5.

All three components, the sprayer and both LEDs, are turned on at the same time. For the Tx video, the number of frames between the LED turning on and the first particles leaving the nozzle denotes the transmission offset Δn_{Tx} . Similarly, on Rx side, the number of frames between the LED turning on and the first particles hitting the center of the frame denotes the Rx offset Δn_{Rx} . The camera has a frame rate f_{cam} . Together with the distance d between Tx and Rx the velocity can be computed as

$$v = \frac{d}{(\Delta n_{Rx} - \Delta n_{Tx}) \cdot f_{cam}}. \quad (2)$$

The obtained velocity of this setup for a distance of 117 cm is 12.77 m/s with an error of around 0.3 m/s due to the frame rate of the used camera (480 FPS). The resulting interval contains the outcome of the previous experiment and therefore confirms the assumption of simulating the testbed particles with a

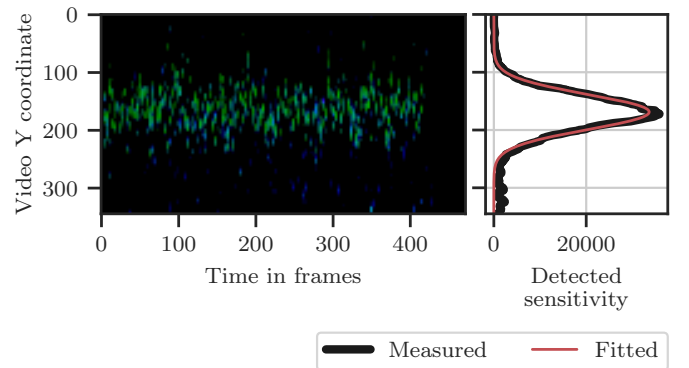


Fig. 6: Heat map and distribution of particles from the receiver's perspective at a distance of 88 cm to the injector.

constant velocity. So, the more precise value of 12.82 m/s denotes v_{init} for the calibrated spray nozzle model. Another observation made from the evaluation of the video footage is that for larger distances, the jet loses its formation and *spreads* or *splits* into several parts with slightly different velocities. The video does not provide enough information for describing these differences in more detail. Nevertheless, to consider this effect in the model, particles should also have slight differences in their initial velocity, which can be modeled by using a normal distribution $\mathcal{N}(\mu = v_{init}, \sigma)$. As there is no experiment to determine σ , variation of this parameter is used to approximate testbed results. It must also be mentioned that although the camera with a frame rate of 1000 FPS is more accurate in determining the velocity of the released droplets from the sprayer, the camera with frame rate of 480 FPS is preferred as Rx for detection purposes. This is because the 480 FPS camera is capable of recording much longer transmission sequences as compared to 1000 FPS camera, which has a much shorter recording time.

Previous experiments do not give an insight into the spatial distribution of particles. So, in another setup, the spray nozzle injects particles for a longer period of time (approximately 1 s) and Rx is placed at different distances. Particles travel through the obtained Rx video—which uses landscape format with a 16:9 aspect ratio—from left to right. By taking the central column of the video for each frame and appending it to a new image, it is possible to generate a heat map of the particles at the corresponding row of the video over time. When summing up all values of a row, this heat map reveals the distribution of particles. Fig. 6 outlines this experiment for a distance of 88 cm. Subtracting the first frame from all others improves the quality as it cancels out constant disturbances like reflections of the light source on the ground. In addition, pixels below a given threshold are marked as black to imitate a noise gate. The curve approximates a normal distribution. So, it becomes possible to replace the distribution \mathcal{P} in Eq. (1) by $\mathcal{N}(\mu, \sigma)$ with $\mu = 0$, since the position of the injector is a separate attribute, and an estimated $\sigma = 1.55$ for the given nozzle.

In the simulation environment however, ejecting only a single particle per time step leads to a fairly large distance between each successively released particles as shown in

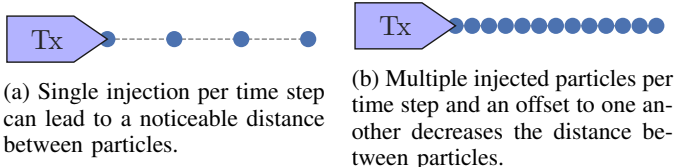


Fig. 7: Distance between particles for the same step size, using a single and multiple injections per time step.

Fig. 7a. This does not reflect the expected water jet shape as a contiguous chain of small droplets. One possibility to solve this issue is to set the step size of the simulator rather small. This however, leads to an increase in overall simulation time needed to emulate the real-life particle injection scenario. In order to avoid this, the injector is made to inject a chain of multiple particles per time step, while computing an even offset to each subsequent chain. This approach ultimately leads to a smaller distance between each successive particle, as shown in Fig. 7b.

It is to be mentioned that the testbed is also designed to accommodate multiple Tx's in order to implement higher order modulation schemes. In this work, those higher order modulation schemes are considered that require two Tx's (discussed in Sec. IV). The sprayer nozzles of the Tx's are separated by a distance of 16 cm. In the Pogona simulator, the same configuration is replicated by the addition of an extra Tx with the said separation distance. However, the approach to model each of the Tx in a two Tx configuration in Pogona simulator is the same as the system using one Tx.

C. Transmission Channel

The transmission channel consists of a tube of diameter 50 cm and a length of 2 m which may be extended further by attaching additional tubes. The tube consists of three rows of six opening flaps, each separated from its neighbor by a distance of 30 cm. The detection and the UV light chambers are mounted on these flaps at varying distances from the Tx for detection purposes. The aluminium frame forms the support structure on which the tube rests. The tube is tilted by a certain angle so as to facilitate proper drainage of the residual solution outside the tube. To further prevent any noise contribution by the residual dye solution, an offset removal technique is employed as described in Sec. V. With the flaps closed, the internal environment of the tube is left completely dark in order to avoid interference from the environmental light.

The simulator moves the particles in discrete time steps. When the particles are injected inside the tube in a jet-spray form, they reach the field of view of the camera at the Rx side, without undergoing any collision with the walls of the tube. This is because the camera at Rx side is positioned along the length of the tube. Therefore it mainly focuses on those particles that majorly pass through the longitudinal centre of the tube, with the walls of the tube lying outside its field of view. So, the channel used for the simulation can be considered to be unbounded. When the particles move through the air, several effects influence their movement like gravity and air drag. These effects however, can be neglected as the changes in

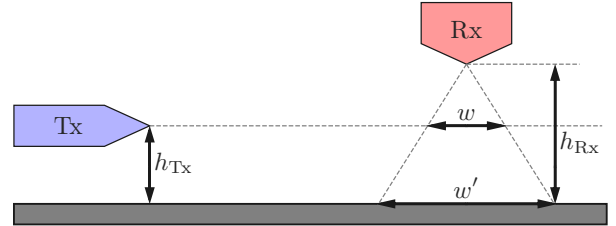


Fig. 8: Experiment to estimate the view of the camera.

the velocity components brought by these effects are nominal, considering the distance the particles travel inside the tube between Tx and Rx in a low viscosity medium.

The new position of each particle $\vec{p}_{n,\text{pos}}$ at time step n, pos is calculated from its previous position $\vec{p}_{n,\text{pos}-1}$, its velocity \vec{v} , and the step size Δt as

$$\vec{p}_{n,\text{pos}} = \vec{p}_{n,\text{pos}-1} + \Delta t \cdot \vec{v}. \quad (3)$$

D. Receiver

The Rx consists of a high-speed digital camera capturing the images of the spray droplets passing through the transmission channel at 480 FPS with a resolution of 1280×720 pixels. The region in focus of the camera is illuminated by an 18 W UV-A flashlight in order to excite the liquid droplets containing the Uranine and Rhodamine 6G molecules. This is seen from the spectrometer measurements in Fig. 3, and described in Sec. V in detail. Fig. 9a and Fig. 9b show Uranine and Rhodamine 6G droplets, respectively, along with the red and green pixel intensity values, when sprayed through the tube, illuminated by the UV-A light source, and viewed by the camera Rx. It is also worth mentioning that the light intensity could also be directly related to the dye concentration as shown in [38]. In order to mimic multiple Rx, the field of view of the camera is divided into multiple spatially separated areas both in the testbed as well as in the Pogona simulator.

By placing the camera on top of the tube while facing downwards, the view of the camera is limited. To estimate the dimensions of this view—its height and width—to be reproduced in the simulation, Fig. 8 helps to compute these values. As it is possible to measure h_{Tx} and h_{Rx} as well as w' (by marking and measuring the edges of the view at the bottom of the tube), the intercept theorem allows to calculate the width of the view w . The aspect ratio of the camera enables to calculate the height h based on the width.

One approach to model Rx in a particle-based simulator is a simple *counting sensor* which counts the number of particles within this specific region. However, this would not incorporate the effect of overlapping particles. So, the simulator generates a video from the camera's perspective which depicts the particles. In the same way, the post-processing script computes the received signal strength from the video footage of the testbed camera, it is possible to apply this script on the generated footage. This leads to a two-step reception process for simulations: (i) generating a video from Rx perspective and (ii) detecting the signal strength by post-processing this video. As the script for step (ii) is already given, the focus

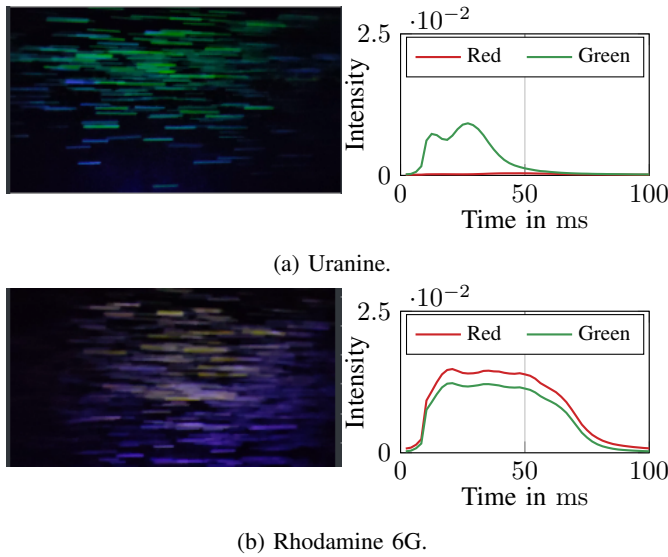


Fig. 9: Rx camera snapshot of water-based solution droplets of Uranine in (a), and Rhodamine 6G in (b) on the left-hand side, with corresponding averaged received signal for $T_{\text{on}} = 20$ ms at $d = 117$ cm on the right-hand side.

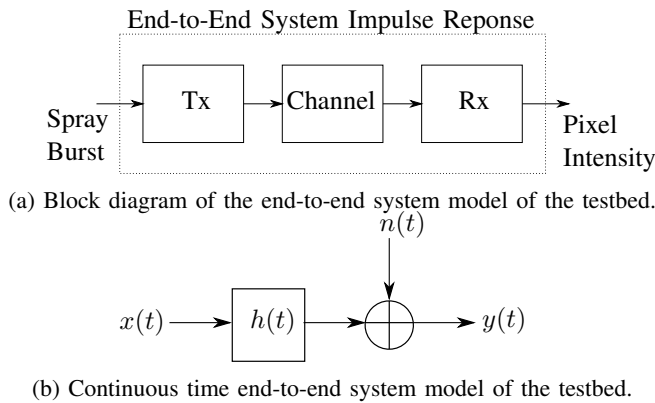


Fig. 10: End-to-end system model of the testbed.

of the simulator lies on the generation of the video. In this work, the video is generated by using the 3D capabilities of Matplotlib.

III. END-TO-END SYSTEM MODEL

The testbed setup can be transformed into a system model in Fig. 10a, as shown in [39], [40]. Therefore, the end-to-end SIR is evaluated by transmitting a short spray burst through the system, resembling a Dirac delta function, and measuring the response using the camera-based detector at the Rx side. In an ideal scenario, the end-to-end SIR comprises of the influences of a perfect Tx, a perfect channel and a perfect Rx on the Dirac delta function. However, the response of the system over multiple trials shows randomness, which may be attributed to the following: imperfect sprayer at the Tx side, turbulence created by the initial interaction of released high velocity droplets with air, the air drag from the transmission channel medium, the uncertainty in the amount of droplets passing through the UV-A light cone, and the imperfection

of the camera-based detector at the Rx side. Some of the sources of randomness are also in line with the noise sources of the MC systems described in [40], [41]. In this section, for a continuous time input $x(t)$ into the system, the ideal end-to-end SIR $h(t)$ along with the noise model $n(t)$ is presented to give the complete analytical end-to-end system model $y(t)$, as described in Fig. 10b.

A. Ideal End-to-End System Impulse Response

The detection is performed using a high-speed digital camera. The spray pulses are recorded which are assumed to be Gaussian-shaped in the time-domain [42], [43], which is in line with the model on alcohol-based MC testbed in [40], with a detailed description about the model coefficients in terms of their true physical meanings in [39]. Thus, the analytical model for the ideal end-to-end SIR without the noise is given as

$$h(t) = \frac{a}{b\sqrt{2\pi}} \exp\left(-\frac{(t-t_0)^2}{2b^2}\right), \quad (4)$$

where a is the intensity from the detected droplets with some attenuation factor, b is the spreading of the pulse in time-domain, while t_0 is the center or the mean of the Gaussian pulse. The goal is to determine the variation of coefficients a and b with distance between Tx and Rx for testbed measurements and simulation data.

The parameters used in the experiment are listed in Table I. For each distance, the measured end-to-end SIRs from the testbed measurements as well as the Pogona simulator measurements are averaged over 60 trials. One example of the 60 measured end-to-end SIRs of the testbed before averaging is shown in Fig. 11. Finally, the analytical model in (4) is fitted through the averaged end-to-end SIR over the considered sample points. The fitting is performed using the non-linear least squares curve-fitting algorithm, as seen from Fig. 11, resembling a Gaussian curve.

The average measured end-to-end SIRs from the testbed, the curve-fitted analytical model and the simulation model are shown in Fig. 11. As it is a challenge to determine the zero time-stamp of the testbed data, synchronizing it with the simulation data is done by aligning the rising edges of the received signals. The maximum value of the simulation data is scaled to match with the maximum value of the testbed. This is necessary since the testbed illumination is inconsistent between distances, which the simulation does not account for.

For a distance of 58 cm, the measured end-to-end SIR of the testbed data is skewed at the beginning of the peak. When the first droplets are released out of the nozzle, a “blob”-like formation as depicted in Fig. 4a forms due to inertia causing

TABLE I: Simulation parameters used for analysis.

Parameter	Value
Symbol duration T	0.05 s
Spray duration T_{on}	0.02 s
Distance to the Rx d	58, 88, 118, 148 and 178 cm
Spray pressure	3 bar
Spray volume rate	0.54 L/min
Camera frame rate	480 FPS

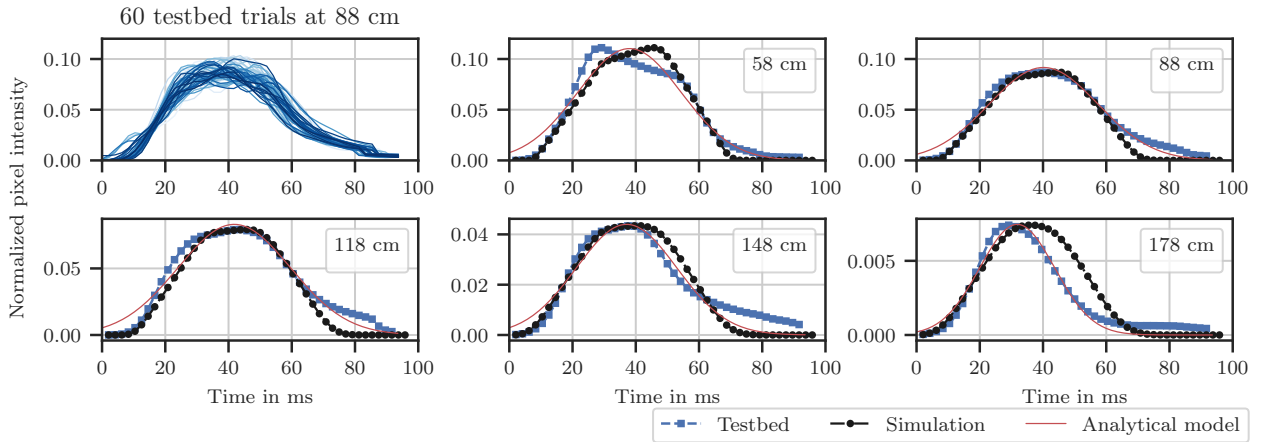
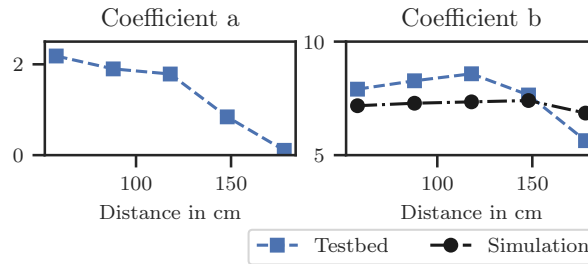


Fig. 11: End-to-end SIRs for different distances.

Fig. 12: Variation of coefficients a and b with distance.

a conglomeration of smaller droplets. As the droplets travel farther, the “blob” eventually spreads out and disintegrates into smaller droplets, reducing its effect at higher distances. This blob is not considered in either model, which is expected to cause deviation from the testbed results.

For the rising edge, the simulator tends to approximate the testbed behavior better than the analytical model. However, the rising edge of the simulated data is still less steep as compared to the testbed data. A more precise estimation of the initial velocity distribution might improve this mismatch.

The testbed signal has an additional tail after the falling edge of the peak, potentially caused by slower particles. This becomes more obvious with increasing distance between Tx and Rx. One reason for this deviation is the air drag, which slows down particles in the testbed. Another issue is the switching process of the spray nozzle, which is not instantaneous as assumed in the spray nozzle model.

Fig. 12 shows the change in magnitude of coefficient a with distance. The value decreases almost linearly with increasing distances. This is attributed to the fact that there is a reduction in the number of droplets traversing the length of the tube, as some droplets either fall down or get dispersed laterally. This increases the distance between the droplets and the camera for higher distances, resulting in a reduction of the light intensity received by the camera. Some droplets might even collide with the enclosing tube and therefore not reach the detector at all. As currently neither gravity nor the influence of light or tubing are modeled in the simulation, the coefficient a is not

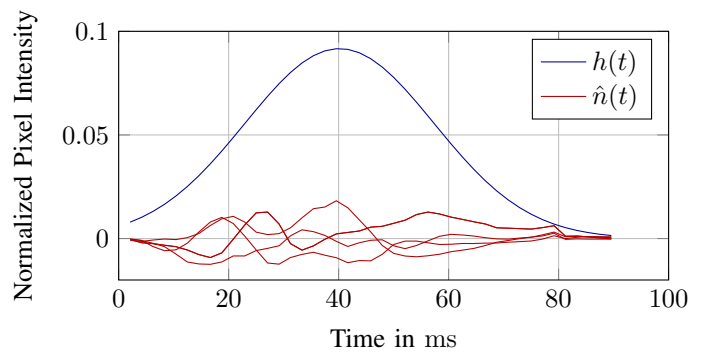


Fig. 13: Ideal end-to-end SIR and estimated noise signal of 5 testbed trials at 88 cm.

calculated for the simulation.

The value of coefficient b increases initially up to 118 cm and decreases afterwards, as shown in Fig. 12. This corresponds to a reduced peak width observed in the testbed at higher distances. The parabolic trajectory decreases the distance between droplets and light source, decreasing consequently the duration of particles being illuminated before leaving the light cone again. The camera, therefore, detects only a smaller part of the pulse actually getting illuminated, giving the impression of the signal with a lower time-domain spread. This problem is worsened by the necessary video de-noise filtering, which might also filter out some less well-illuminated droplets entirely. Together, these effects could account for the difference between simulation and experiment.

B. Noise Model

In the following, a noise model is designed that emulates the randomness present in the system, which together with the proposed analytical model of the ideal end-to-end SIR in (4), provides the complete analytical end-to-end system model of the testbed. This model could then be used to predict results from time-consuming testbed measurements by conducting extensive simulations.

The proposed noise model is assumed to be additive in nature. In order to establish it, the noise samples in m

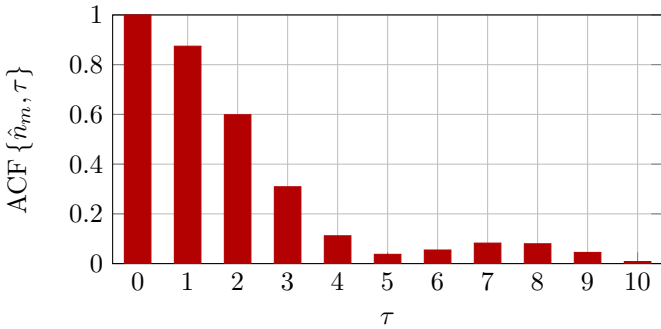


Fig. 14: Averaged ACF of estimated noise signal at 88 cm.

multiples of period $T_{\text{cam}} = 1/f_{\text{cam}}$ are estimated. Therefore, the estimated noise sample \hat{n}_m from the measured end-to-end SIR trials $h_{\text{meas}}(t)$ and the ideal end-to-end SIR sampled at $t = mT_{\text{cam}}$, is given as

$$\hat{n}_m = h_{\text{meas}}(mT_{\text{cam}}) - h(mT_{\text{cam}}). \quad (5)$$

In Fig. 13, the estimated noise signals of five testbed trials at a transmission distance of 88 cm is shown as an example. By the shape of the noise signals and a comparison to the ideal SIR, it is observed that the noise power is amplitude-dependent and the individual noise samples show a statistical dependency on previous noise samples. The former property also applies to the diffusion noise in classical diffusion-based MC models [44]. Motivated by the diffusion noise in the literature and supported by the central limit theorem, which states that the superposition of uncorrelated random variables in real-life scenarios roughly leads to a Gaussian distribution, the noise process variance can therefore be modeled as an amplitude-dependent white Gaussian noise:

$$\sigma_n^2(t) = h(t)(1-h(t)). \quad (6)$$

The statistical dependence of the estimated noise sample \hat{n}_m to a previous noise sample $\hat{n}_{m-\tau}$, with a relative time lag of τ is described by the auto-correlation function $\text{ACF}\{\hat{n}_m, \tau\}$. This function is illustrated as an exemplary in Fig. 14 for a transmission distance of 88 cm. It is observed that the main contribution of the statistical dependence with ACF weight of at least 0.1 originates from the four previous noise samples, which makes them correlated in nature. This is in contrast to a white noise process, where the statistical dependence of a noise sample on any of the previous noise samples is absent. It is to be noted that the strong correlation between the current sample and the past noise samples exists due to the fact that the same droplets appear multiple times in a sequence of recorded frames of the camera, as they travel along the camera's field of view. Once the droplets exit the field of view of the camera, there is no longer any contribution by these droplets to the pixel intensity values, recorded in subsequent frames. The observation is also true for the other transmission distances under investigation. As a consequence of these observations specific to the testbed design, the statistical dependence of the

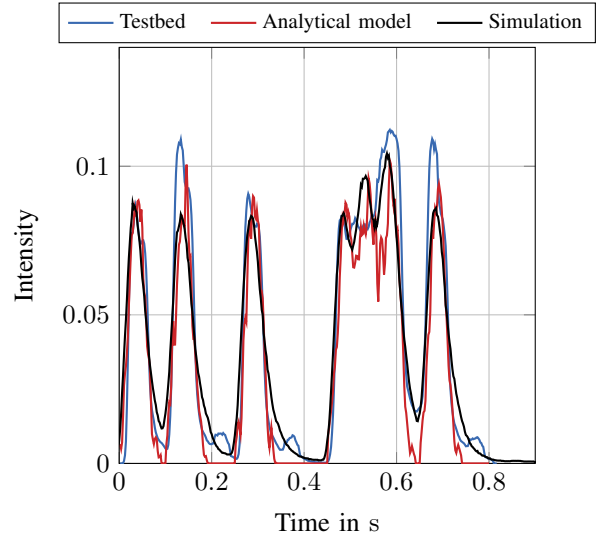


Fig. 15: OOK modulated transmission of letters “ICT” in binary equivalent form at 88 cm.

noise samples is given by a simple autoregressive (AR) model of order 4:

$$n_m = \frac{1}{\sqrt{\left(1 + \sum_{i=1}^4 \phi_i^2\right)}} \left(\sum_{i=1}^4 \phi_i n_{m-i} + \varepsilon_m \right), \quad (7)$$

where ϕ_i are the weight factors that determine the influence of the previous noise samples, and $\varepsilon_m \sim \mathcal{N}(0, 1)$, is a zero-mean white Gaussian noise process with a variance of 1. The parameters of the AR model are determined from the measured testbed signals in the sense of a maximum likelihood estimation. The amplitude-dependent noise process can be given as

$$n(mT_{\text{cam}}) = \sigma_n(mT_{\text{cam}}) \cdot n_m. \quad (8)$$

Finally, the analytical model for the complete end-to-end system can be described conforming with Fig. 10 as

$$y(mT_{\text{cam}}) = x(mT_{\text{cam}}) * h(mT_{\text{cam}}) + n(mT_{\text{cam}}), \quad (9)$$

where $*$ represents the convolution operation.

C. Data Transmission

The data transmission of the text message “ICT” using an OOK modulation scheme with Uranine-water-based solution is shown in Fig. 15. A source coded bit sequence “010010001110100” corresponding to the ASCII code of the transmission text is sent over the testbed channel. An initialization bit “1” precedes the transmission sequence in order to facilitate proper synchronization at Rx side. The same text message is transmitted using the analytical and the Pogona simulation models as also shown in Fig. 15. It is seen that the models very closely emulate the result obtained from the testbed. The plot from the Pogona simulator, however, shows a comparatively larger ISI as compared to the plot obtained from the analytical model.

IV. MODULATION SCHEMES

This section presents the various modulation schemes implemented at the Tx side of the testbed based on a single or multiple fluorescent dyes. The list is not complete but includes most of the common modulation schemes considered in MC literature.

A. On-Off Keying

OOK is a simple modulation scheme, and therefore widely used in MC. The binary information is represented by molecules released at Tx or by their absence. Therefore, a single type of molecule is sufficient. In the testbed, only a single sprayer is used, which contains a Uranine-water-based solution. For a binary “1”, the solenoid valve of the sprayer is opened for $T_{\text{on}} = 20$ ms at the beginning of a transmission interval, while it remains closed for a binary “0”. The spray time of $T_{\text{on}} = 20$ ms is chosen as it is the shortest possible time during which the sprayers with the solenoid valves produce clear spray jets. During this time period, the volume of the water-based dye solution sprayed is $V_{\text{on}} = 0.18$ mL. The symbol duration $T = 50$ ms is chosen so as to minimize the effect of ISI and to have distinguishable pulses with a complete cycle of opening and shutting of the solenoid valve (minimum shutting time of the valve is 30 ms) [22].

B. Pulse Position Modulation

Pulse position modulation (PPM) is a technique where M data symbols are encoded by transmitting a pulse occupying one of the M chip slots of duration T_c within a symbol duration $T = M T_c$. Bearing in mind the Tx hardware restrictions, suitable T_c is chosen. For this work, $T_c = 25$ ms is considered as with this chip duration, it is still possible to produce distinguishable pulses with a complete cycle of opening and shutting of the solenoid valve (minimum shutting time of the valve is 30 ms). Here, 2, 4, and 8-ary PPM are implemented using Uranine-water-based solution.

C. Differential Pulse Position Modulation

Differential pulse position modulation (DPPM) [45] is implemented by transmitting a reference pulse of duration $T_{\text{on}} = 25$ ms, with each of the M subsequent symbols being transmitted with same pulse duration after a certain time gap, in multiples of $T_{\text{off}} = T_{\text{on}} = 25$ ms from the previous pulse. The symbol in M -ary DPPM is represented as $s_i = i T_{\text{off}}$, $i \in \{0, \dots, M - 1\}$. In this work, however, 2, 4, and 8-ary DPPM are implemented using Uranine-water-based solution.

D. Shorten Pulse Position Modulation

Shorten pulse position modulation (SPPM), as first shown in [46], is a modulation technique where the first bit of an M -ary scheme is OOK modulated while the remaining bits are PPM modulated. This makes it more bandwidth efficient as compared to standard PPM. The chip duration $T_c = 25$ ms while symbol duration $T = \left(2^{\log_2 M - 1} + \text{mod}(2^{\log_2 M - 1}, 2) + (\sqrt{-1})^M\right) T_c$. Uranine-water-based solution is used in this work to implement 2, 4, and 8-ary SPPM.

E. Multi-pulse Pulse Position Modulation

Contrary to PPM, where one pulse occupies one of the M chip slots for modulating a symbol in an M -ary system, in multi-pulse pulse position modulation (MPPM) scheme, several pulses occupy the chip slots to represent one symbol in an M -ary system [47]. If K_c among N_c chip slots are to be occupied by the pulses to represent a symbol, then up to $\binom{N_c}{K_c}$ symbols can be transmitted. However, the value $\binom{N_c}{K_c}$ is not a power of two and in order to transmit $\log_2 M$ bits, the additional symbols must be modulated by conventional PPM technique using a single pulse. In this work, the value of $N_c = 4$, $K_c = 2$ and 8-ary MPPM is implemented with a symbol duration $T = M T_c / p$, where $p = 2^{\log_4(M/2)}$ and the chip duration is $T_c = 25$ ms.

F. Molecular Shift Keying

MoSK is a modulation scheme where different types of molecules are used to represent different symbols based on their distinguishability by Rx. Based on this idea, multiple fluorescent dyes are released from the Tx-side sprayers which emit light of different wavelengths under the influence of the UV light source. In this paper, 2-ary MoSK is implemented and is realized by two sprayers, one filled with a Uranine-water-based solution and the other filled with a Rhodamine 6G-water-based solution. For a binary “0”, the solenoid valve of the Uranine-water-based solution is opened for $T_{\text{on}} = 20$ ms at the beginning of the transmission interval. Similarly, for a binary “1”, the solenoid valve of the Rhodamine 6G-water-based solution is opened for the same duration. The symbol duration is $T = 50$ ms.

G. Molecular Concentration Shift Keying

MCSK combines the idea of different concentration levels and type of molecules to form higher-order modulation schemes. The different types of molecules are modulated in two different concentration levels respectively and transmitted simultaneously. 4-ary MCSK is realized in this work by the Uranine-water-based solution and the Rhodamine 6G-water-based solution by modulating the sprayers according to OOK and transmitting them in such a way that either both the sprayers are switched off, or one of them is switched on, or both the sprayers are switched on for a period of $T_{\text{on}} = 20$ ms with a symbol duration $T = 50$ ms. Thus, up to four different combinations can be made to represent four different transmitted symbols, each consisting of two bits. Here, two different dimensions in the form of concentration levels and different types of dyes are exploited resulting in higher degree of freedom and higher bandwidth efficiency.

H. Spatial Shift Keying

Spatial shift keying (SSK) [27], [29] is a modulation scheme where the symbols are represented based on the visibility of molecules in a particular region of space. Based on this idea, the fluorescent dye is released from the Tx-side sprayer nozzles, which are separated by a distance of 16 cm. The alignment ensures the visibility of most droplets being sprayed

out by the Tx's in one of the sections of the field of view of the Rx camera. Based on this principle, a decision about the transmission of a particular symbol is made. In this work, 2-ary SSK is implemented where the binary information is represented by the use of two different sprayers, both filled with Uranine-water-based solutions. For a binary “0”, the solenoid valve of the sprayer is opened for $T_{on} = 20$ ms, for which the upper half region of the field of view of the camera Rx receives most of the sprayed fluorescent droplets. Similarly, for a binary “1”, the lower half region of the field of view of the camera Rx receives most of the sprayed fluorescent droplets. The symbol duration is $T = 50$ ms.

I. Spatial Concentration Shift Keying

Similar to MCSK, spatial concentration shift keying (SCSK) combines the idea of different concentration levels along with the visibility of the molecules in a particular region of space, to form higher-order modulation schemes [28]. This concept is very similar to the idea of spatial multiplexing in multiple-input-multiple-output systems [48]. 4-ary SCSK is implemented in this work by filling up both the sprayers with Uranine-water-based solutions and aligning them in two different configurations. The released dye solutions from Tx side are modulated according to OOK, and sprayed in such a way that either both the sprayers are switched off, or one of them is switched on, or both the sprayers are switched on for a period of $T_{on} = 20$ ms with a symbol duration $T = 50$ ms. This results in the released droplets being not visible at all, or the droplets being visible in the lower half, upper half or in both the regions of the field of view of the camera Rx. Thus, up to four different combinations can be made possible to represent four different transmitted symbols. This results in a 4-ary modulation scheme, with each symbol comprising of two bits. Here again, two different dimensions in the form of concentration levels and spatial configurations are exploited resulting in higher degree of freedom and higher bandwidth efficiency.

J. Comparison

Given all the hardware restrictions, the general expressions for the achievable data rate R and the average volume sprayed per bit V for the implemented modulation schemes are listed in Table II. These metrics may be chosen in accordance with the design criteria. For example, if V is not crucial, the design goal may be to maximize R . On the other hand, V may be considered as a design criterion if resources are limited and R is not pivotal. A performance comparison of the modulation schemes based on the aforementioned parameters is essentially gauged by increasing the data symbol cardinality M . Fig. 16 shows the variation of R with M and it is seen that for the modulation schemes using a single dye as the information carrier, a general trend is observed where R increases or remains the same up to a certain point before gradually decreasing with M . This is because the symbol duration T increases with M and its effect is more dominant as compared to the number of bits transmitted per symbol. This observation is, however, not seen in schemes such as MoSK,

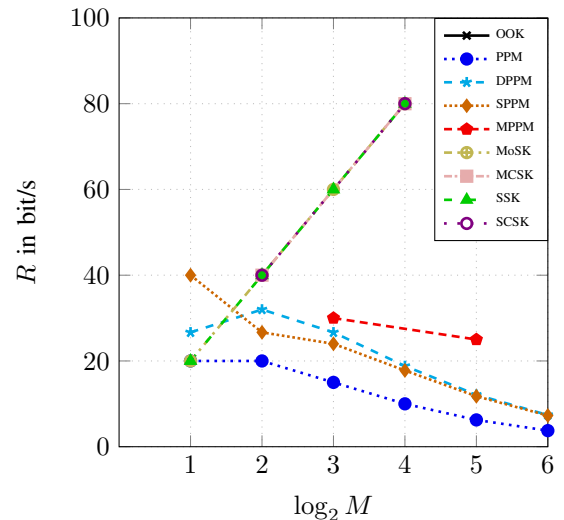


Fig. 16: Variation of achievable data rate R with symbol cardinality M .

MCSK, SSK, and SCSK, as the symbols are represented by multiple dimensions in terms of fluorescent dyes, space, and concentration levels.

Similarly, Fig. 17 depicts the variation of the average volume sprayed per bit V with symbol cardinality M . Most modulation schemes display a common characteristic where, occasionally, V increases up to a certain value of M and there onward, decreases. This, however, is not true for modulation schemes such as MCSK and SCSK as seen from the expression for V , which display an ever increasing trend.

A more meaningful performance metric is, therefore, the ratio of achievable data rate R and average volume sprayed per bit V given by R/V , which takes into account both the design criteria. It is seen that for modulation schemes using a single dye as information carrier, R/V increases up to a certain point and then decreases. This is because with increase in symbol cardinality M , the influence of parameter V dominates over the influence of parameter R . However, this is not true for the schemes using multiple dyes as information carriers such as MoSK, MCSK, SSK and SCSK as the influence of parameter R is more dominant than the influence of parameter V .

V. DETECTION

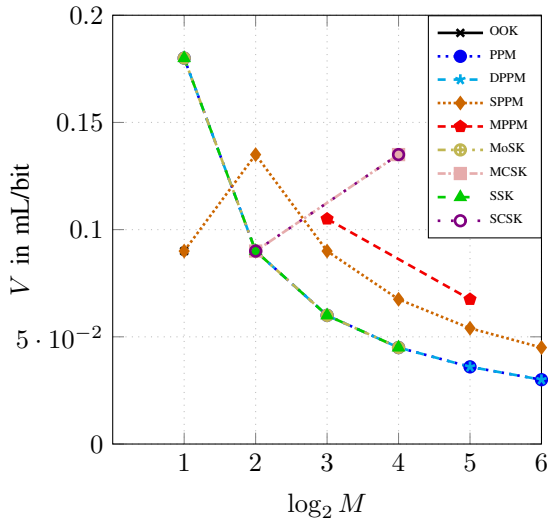
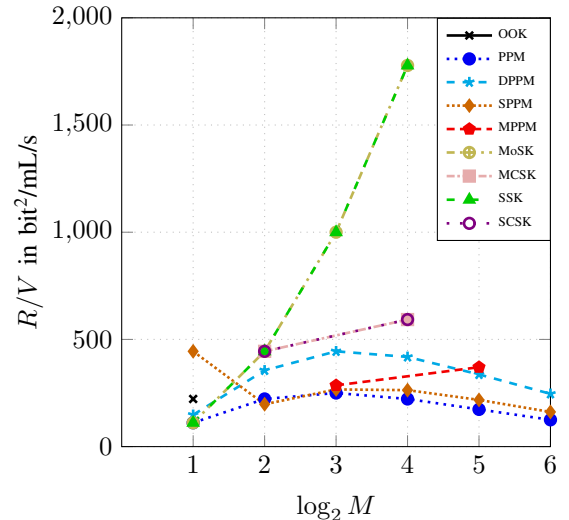
In this section, the overall receiver-side detection process is described in detail along with the detection algorithms with their BER performance comparison. The investigation is performed on the testbed measurements, the analytical model simulation results, as well as the Pogona simulator results.

A. Detection Process

1) *Video Post-Processing:* Prior to detection, the videos recorded by the high-speed camera are post-processed. In a first step, a reference frame, recorded before the actual transmission, is subtracted from all frames of the video to avoid any offset caused by luminous components within the

TABLE II: Achievable data rate R with average volume sprayed per bit V with increasing cardinality M .

Modulation	R	V
OOK	$\frac{1}{T}$	$\frac{V_{\text{on}}}{2}$
PPM	$\frac{\log_2 M}{M T_c}$	$\frac{V_{\text{on}}}{\log_2 M}$
DPPM	$\frac{2 \log_2 M}{T_{\text{off}} (M - 1) + 2 T_{\text{on}}}$	$\frac{V_{\text{on}}}{\log_2 M}$
SPPM	$\frac{\log_2 M}{(2^{\log_2 M - 1} + \text{mod}(2^{\log_2 M - 1}, 2) + (\sqrt{-1})^M) T_c}$	$\frac{\left(\frac{M}{2} + 2 \left((2^{\log_2 M - 1} + \text{mod}(2^{\log_2 M - 1}, 2) + (\sqrt{-1})^M) - 1\right)\right) V_{\text{on}}}{M \log_2 M}$
MPPM	$\frac{\log_2 \left(\binom{M/p}{2} + p\right)}{M T_c / p}$, where $p = 2^{\log_4(M/2)}$	$\frac{\left(2 \binom{M/p}{2} + p\right) V_{\text{on}}}{M \log_2 M}$, where $p = 2^{\log_4(M/2)}$
MoSK	$\frac{\log_2 M}{T}$	$\frac{V_{\text{on}}}{\log_2 M}$
MCSK	$\frac{\log_2 M}{T}$	$\frac{M(\sqrt{M} - 1)V_{\text{on}}}{M \log_2 M}$
SSK	$\frac{\log_2 M}{T}$	$\frac{V_{\text{on}}}{\log_2 M}$
SCSK	$\frac{\log_2 M}{T}$	$\frac{M(\sqrt{M} - 1)V_{\text{on}}}{M \log_2 M}$

Fig. 17: Variation of average volume sprayed per bit V with symbol cardinality M .Fig. 18: Variation of ratio R/V with symbol cardinality M .

tube. In a second step, the intensities of the red and green pixels of each frame are summed separately, which serve as input signal for detection.

2) *Intercolor Interference Cancellation:* While Uranine under UV-A light has mostly green component, Rhodamine 6G appears rather yellowish, which is represented by approximately equal green and red components (see Fig. 9). Therefore, when both the dyes are used simultaneously, there is inter-color interference (ICI) in the green received signal, which significantly reduces the detection performance. To counteract this effect in 2-MoSK and 4-MCSK, the red received signal is subtracted from the green received signal before detection. This property helps to distinguish between the dyes sprayed, which helps to improve the BER perfor-

mance or the bit rate.

3) *Energy Detection:* In the sense of energy detection, the red and/or the green pixel intensity value acts as the received signal and is integrated over symbol duration T . The ℓ th end-to-end system coefficient h_ℓ , $0 \leq \ell \leq L$ is calculated as

$$h_\ell = \int_{\ell T}^{(\ell+1)T} h(t) dt, \quad (10)$$

where L is the effective end-to-end system memory length. Therefore, the relation between the transmitted symbols $x[k]$ and the pixel energy values $y[k]$ over T can be exactly described in discrete-time domain by a convolution operation with addition of noise term $n[k]$ in the form of equivalent

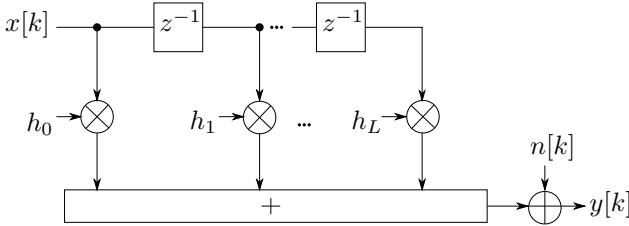


Fig. 19: Equivalent discrete-time end-to-end system model.

discrete-time end-to-end system model [44], as shown in Fig. 19.

B. Detection Algorithms

The various detection algorithms are employed at the Rx side and a performance comparison in terms of BER is presented. The equalization techniques form a part of certain detection algorithms, which help reduce the BER by removing the ISI. It is worth mentioning that the detection processes employing equalizers require the estimate of the end-to-end system coefficients. The $L + 1$ end-to-end system coefficients are estimated using least squares channel estimation method. For a noise-free scenario, a pilot matrix \mathbf{A} of size $(L + 1) \times K$ and detected energy vector \mathbf{y} of size $1 \times K$, the estimated end-to-end system vector $\hat{\mathbf{h}}$ is given as

$$\hat{\mathbf{h}} = \mathbf{y}\mathbf{A}^\top (\mathbf{A}\mathbf{A}^\top)^{-1}. \quad (11)$$

1) Threshold Detection: Threshold detection (TD) is a simple and low-complexity symbol detection technique where the detected energy from the received signal is integrated over the corresponding transmission interval. A decision about the transmitted symbol is made when the received energy sample $y[k]$ exceeds a certain threshold level ξ , which helps to make the decision about $\hat{x}[k]$ for the corresponding transmitted symbol. The value of ξ remains unchanged during the detection process of the entire sequence of symbols in case of fixed threshold detection (FTD) [49]. For binary OOK modulation, the FTD rule is

$$\hat{x}[k] = \begin{cases} 0 & \text{if } y[k] \leq \xi, \\ 1 & \text{if } y[k] > \xi. \end{cases} \quad (12)$$

The threshold is chosen for each distance separately, so that it leads to a minimum BER over all recordings. This detection technique is also employed in 4-MCSK, 4-SCSK and 8-MPPM.

Another TD technique to effectively counteract the effect of ISI is adaptive threshold detection (ATD), where the threshold value ξ changes depending on the received energy sample of the previous transmitted symbol [50]. For binary OOK modulation, the ATD rule is

$$\hat{x}[k] = \begin{cases} 0 & \text{if } y[k] \leq \xi = y[k - 1], \\ 1 & \text{if } y[k] > \xi = y[k - 1]. \end{cases} \quad (13)$$

Without ISI in the channel, ATD performs poorly. However, ATD needs no knowledge of the end-to-end system coefficients

h_ℓ . Modulation schemes such as 2-PPM, 4-PPM, 8-PPM, 2-DPPM, 4-DPPM, 8-DPPM, 2-MoSK, 2-SSK incorporate some form of ATD in their detection process while modulation schemes like 4-SPPM and 8-SPPM use a combination of FTD and ATD in their detection process.

It is also to be noted that in the case of 2-MoSK and 4-MCSK, the signal strengths of the red and green pixel intensity values are very different. Therefore, in order to compensate for the same, the red and green pixel energy values are weighted with a factor inversely proportional to their average signal strengths before the detection process.

2) Zero-Forcing Equalizer: The zero-forcing (ZF) equalizer is a linear equalizer which is helpful in tackling the problem of ISI in the transmission system. When a transmission system is represented by its memory and end-to-end system coefficients as a finite impulse response filter, the ZF equalizer with its filter coefficients g_j is designed in such a way that it acts as an inversion to the end-to-end system, thus, completely eliminating ISI in a noise-free scenario. In time domain, the convolution of the end-to-end system coefficients with the ZF filter coefficients results in a unit impulse [51]:

$$\sum_{j=-\infty}^{\infty} g_j h_{\ell-j} = \begin{cases} 1 & \text{if } \ell = 0, \\ 0 & \text{if } \ell \neq 0. \end{cases} \quad (14)$$

3) Decision-Feedback Equalizer: The decision-feedback equalizer (DFE) is a nonlinear equalizer comprising a nonlinear feedback filter [51]. This helps to cancel out the effect of ISI. The equalized received energy sample $y'[k]$ is given as

$$y'[k] = y[k] - \sum_{\ell=1}^L \hat{x}[k - \ell] h_\ell, \quad (15)$$

where $\hat{x}[k - \ell] h_\ell$ is the estimated ISI, which is subtracted from the received energy sample $y[k]$. The transmitted symbol estimate $\hat{x}[k]$ is obtained, after $y'[k]$ undergoes a threshold detection process.

4) Maximum Likelihood Sequence Estimation: The maximum likelihood sequence estimation (MLSE) detector aims at minimizing the sequence error in the detected sequence of symbols. The most likely transmitted sequence in MLSE is determined by considering every possible sequence [51],

$$\hat{\mathbf{x}} = \arg \max_{\tilde{\mathbf{x}}} \{p(\mathbf{y} | \tilde{\mathbf{x}})\}, \quad (16)$$

where $\tilde{\mathbf{x}}$ is the transmitted symbol sequence hypothesis. To elegantly perform MLSE detection, the Viterbi algorithm is used in this particular work, which identifies the most probable path with the help of a trellis diagram [52]. Assuming the Euclidean distance metric, the branch metrics γ for symbol hypothesis $\tilde{x}[k]$ is given as

$$\gamma^{\tilde{x}[k]} = \left| y[k] - \sum_{\ell=0}^L h_\ell \tilde{x}[k - \ell] \right|^2. \quad (17)$$

VI. RESULTS

In this section, the BER performances of the implemented modulation schemes are carried out for the testbed, the analytical model, as well as the Pogona simulator measurement

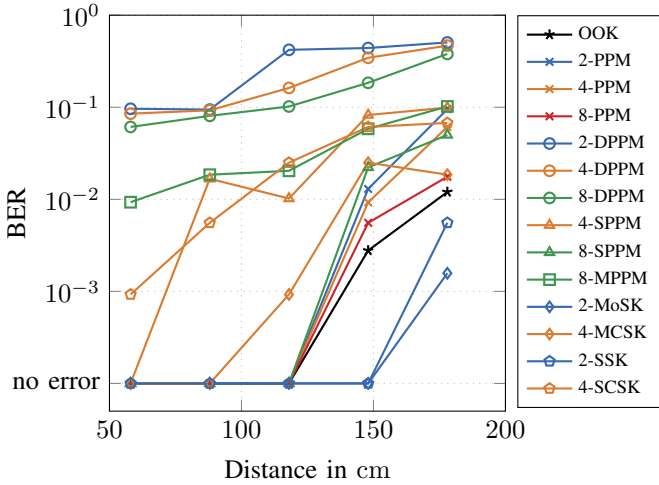


Fig. 20: BER analysis of modulation schemes under investigation with respect to transmission distance. Results are obtained from testbed measurements.

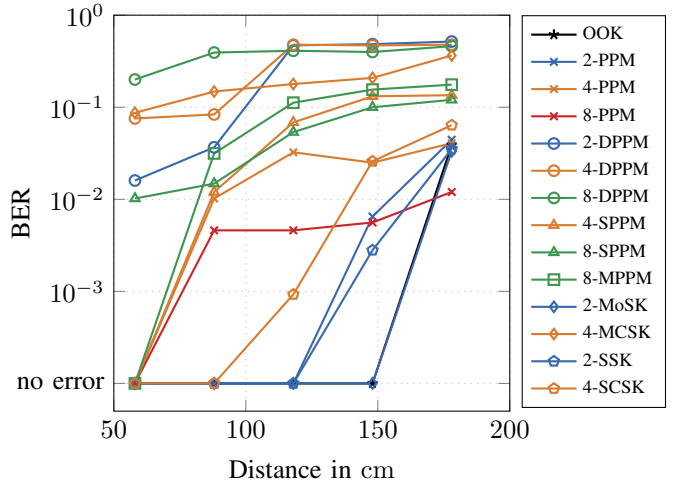


Fig. 22: BER analysis of modulation schemes under investigation with respect to transmission distance. Results are obtained from the Pogona simulator.

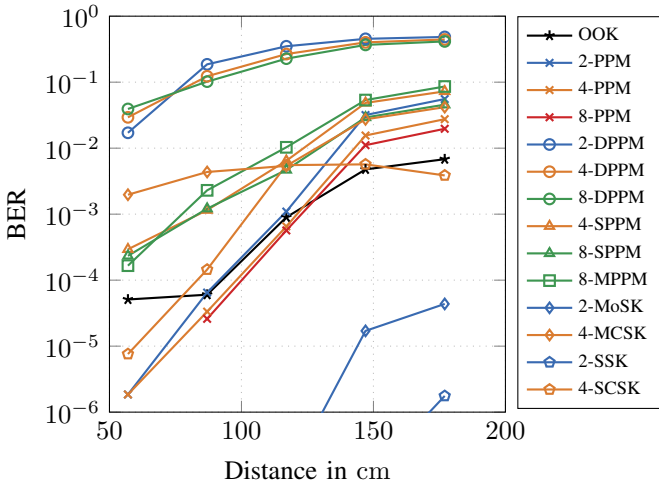


Fig. 21: BER analysis of modulation schemes under investigation with respect to transmission distance. Results are obtained from analytical model simulations.

results. Furthermore, a comparison of the performance of various detection algorithms is also presented. A BER comparison of the implemented modulation schemes and the detection algorithms is carried out according to the parameters listed in Table I, with a data transmission sequence length of 108 bits. In the case of testbed and Pogona simulator measurements, ten trials for every transmission distance are performed due to resource constraints and higher computational time, respectively. A much lower and more accurate BER is achieved in the case of the analytical model (described in Sec. III) as 10^5 trials are carried out for every transmission distance with less computational time and effort.

A. Modulation Schemes

A BER comparison of the implemented modulation schemes is carried out in this section. The transmission sequence length

of 108 bits is chosen in order to make it possible to compare up to $2^4 = 16$ -ary modulation schemes in future work. The symbol duration for most modulation schemes is $T = 50$ ms, while for modulation schemes like PPM, SPPM and MPPM, $T_c = 25$ ms. Similarly, in the case of DPPM, $T_{on} = T_{off} = 25$ ms. The values are chosen in such a way that they ensure transmission of symbols with minimum ISI.

The BER analysis of the modulation schemes for the testbed measurements is given in Fig. 20, for the analytical model in Fig. 21, and for the Pogona simulator in Fig. 22. It is observed as a common phenomenon between the measurement and the simulation environments that the BER performance deteriorates with increase in transmission distance d for every implemented modulation scheme. This is due to the fact that there is a significant reduction in the number of droplets traveling the length of the tube and reaching the field of view of the camera in the case of testbed measurements and analytical model. The droplets either fall down due to the gravitational pull and collect at the bottom of the tube or simply get dispersed laterally. This reduces the intensity of light received by the camera. However, in the case of the Pogona simulator, the effect of gravity is neglected but the particles undergo lateral dispersion with increase in d . This leads to a lower number of particles reaching the Rx side. All these influences decrease the received signal strength while contributing to the noise process.

As seen from the BER plots, DPPM is the worst performer. This is because in DPPM, the time gap between two successive pulses determines the data transmitted. However, the detection of a successive pulse at an undesirable time slot leads to an error and from there onwards, every subsequent pulse detected most-likely falls in an undesirable time slot leading to a massive error propagation.

Although ATD is used in PPM, the BER performance is still worse than that of OOK. This is due to the fact that the fixed chip duration T_c is small, which leads to increased ISI in a chip slot within a symbol duration T for PPM with

lower symbol cardinality M . As M increases, $T = M T_c$ also increases improving the ATD detection process. This, in turn, improves the BER performance.

Modulation schemes such as SPPM and MPPM perform better than DPPM but worse than PPM since these schemes employ a multi-pulse system where more than one pulse is transmitted over multiple chip slots within a symbol duration T , unlike PPM where only a single pulse per T is transmitted. This makes it more difficult for the detector to distinguish the transmitted symbols based on the position of the pulses in chip slots within T , thus increasing the BER. Again, with increase in symbol cardinality M , the BER performance improves as the overall T increases while chip duration T_c remains fixed. This is similar to the case observed in PPM.

4-MCSK performs better than most modulation schemes but worse than OOK due to the influence of ICI. This work, however, attempts to reduce this effect as explained in Sec. V-A2. However, the BER performance of 4-SCSK in the testbed measurements is worse than 4-MCSK due to the presence of inter-link interference (ILI) but shows improvement in the case of analytical model as the ILI is not included.

The BER performance of 2-MoSK is better than that of OOK as with reduction in ICI, the information decoded by Rx is assumed to be obtained from two reliable independent sources (two separate dyes). The dyes represent the same transmitted symbol in complementary fashion, where one dye is sprayed while the other dye is not sprayed. This improves the confidence of the detection algorithm as the information is obtained from both the dyes for a particular event, resulting in improved BER performance. Similar performance is seen in terms of 2-SSK. However, due to the presence of ILI, the performance is worse than 2-MoSK in case of testbed measurements. In the analytical model in Fig. 21, 2-SSK has a better performance as compared to 2-MoSK as the ILI is neglected. In the case of Pogona simulator however, 2-SSK has worse BER performance than OOK. This is due to the fact that the spray jets from two different sprayers are not completely distinguishable at larger distances as the droplets from both the sprayers overlap, closing the spatial gap between the two beams of the spray jets. This causes an erroneous decision at Rx side. The BER performance however, slightly improves in the case of 2-MoSK as the droplets are still distinguishable in terms of color.

The testbed and Pogona simulator measurements are limited in terms of time efficiency and complexity. Hence, analytical models prove to be more reliable when it comes to performing a large number of transmission trials in a shorter amount of time, producing more accurate BER values below 10^{-3} .

B. Detection Algorithms

A comparative BER performance analysis of the detection algorithms for the testbed measurements is shown in Fig. 23. For this investigation, only the Uranine-water-based solution is used. An end-to-end system with a memory length $L = 5$ with OOK modulation scheme is considered. However, the detection algorithms with equalization techniques can easily be extended to the other modulation schemes. For the analysis,

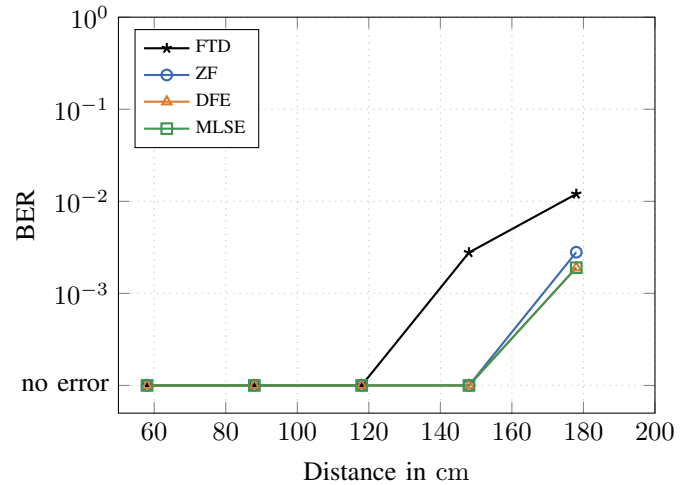


Fig. 23: BER analysis of detection algorithms under investigation with respect to transmission distance. Results are obtained by testbed measurements.

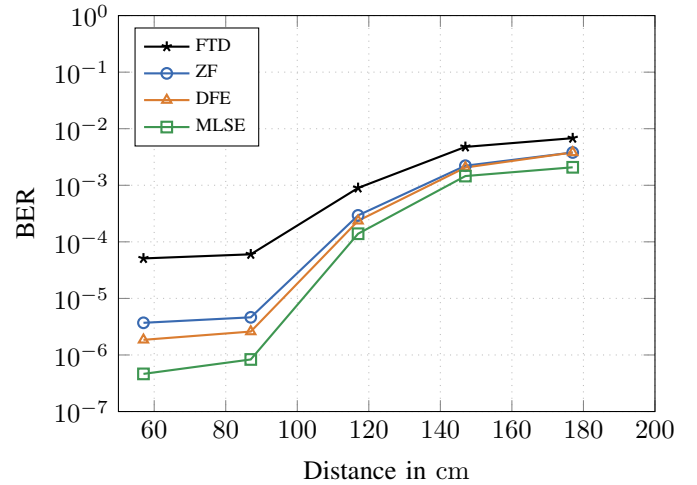


Fig. 24: BER analysis of detection algorithms under investigation with respect to transmission distance. Results are obtained by analytical model simulations.

the filter coefficients length for both ZF and DFE equalizers is considered to be the same as the end-to-end system memory length. The FTD is the worst performer as it does not take ISI into account. The ZF equalizer performs better than the FTD but performs worse than the DFE and MLSE-based equalizers due to the inversion of the end-to-end system when determining ZF equalizer's filter coefficients. Furthermore, noise amplification occurs for smaller end-to-end system coefficients. The DFE, however, only feeds back hard decisions and does not amplify the noise and, therefore, has a better BER performance as compared to the ZF equalizer. However, error propagation might still occur in the case of DFE if a decision is made incorrectly. The MLSE-based equalizer performs as good as the DFE due to its high computational complexity. Similar results are obtained when these detection algorithms are implemented using the analytical model as shown in Fig. 24. In the case of the Pogona simulator, no

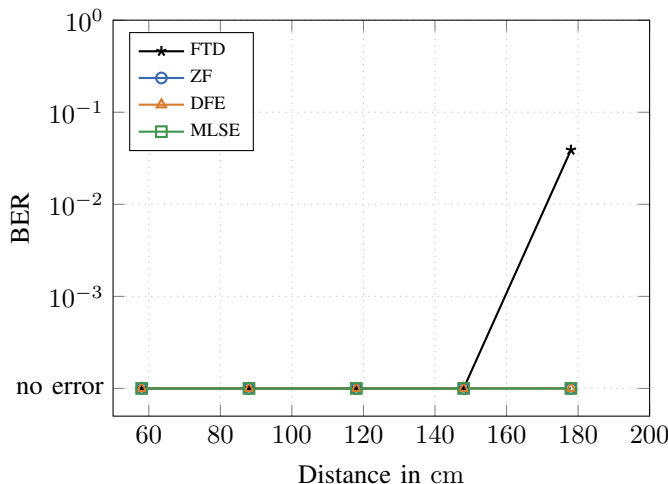


Fig. 25: BER analysis of detection algorithms under investigation with respect to transmission distance. Results are obtained from the Pogona simulator.

errors are seen when all the equalizers are applied as shown in Fig. 25.

For a comparison of the performance of the equalizers below a BER of 10^{-3} , analytical model proves to be more reliable, as a large number of trials can be run in a much shorter period of time to produce the required results, as compared to the testbed and Pogona simulator measurements.

VII. CONCLUSION AND OUTLOOK

In this paper, a macroscopic air-based MC testbed is presented. An industrial sprayer is used as its Tx which releases the information carrier in the form of fluorescent dyes towards a high-speed camera stationed as Rx at a distance d ranging between several tens of centimeters and meters. A detailed analysis of its channel model comprising of the ideal end-to-end SIR and noise model is shown to obtain the complete analytical end-to-end system model. Various modulation schemes with their achievable data rates, resource requirements, and BER performances with higher degrees of freedom using different colors of the dyes and the spatial domain are presented with the measurement results obtained from the testbed, the analytical model, and the Pogona simulator. It is shown that modulation schemes such as 2-SSK and 2-MoSK have the best performances in terms of BER while schemes such as 4-SCSK and 4-MCSK had the best data transmission rates. Furthermore, a comparative study of BER performances of various detection algorithms is performed on OOK measurement results obtained from the testbed, the analytical model, and the Pogona simulator, and it is seen that the FTD has the worst BER performance while the MLSE-based equalizer has the best BER performance.

Future research work will include channel coding schemes and efficient detection algorithms, which would further increase the BER performance by reducing the effects of ISI, ICI, and ILI further from the testbed measurement results. More accurate models of ISI, ICI, and ILI in the case of analytical and Pogona simulator models are to be included

in order to emulate the testbed measurement results as closely as possible. In addition, relaying may be incorporated in order to achieve larger transmission distances without compromising the BER performances.

REFERENCES

- [1] T. Nakano, A. W. Eckford, and T. Haraguchi, *Molecular Communication*. Cambridge, UK: Cambridge University Press, 2013.
- [2] B. Atakan, *Molecular Communications and Nanonetworks*, New York, NY: Springer, 2014.
- [3] N. Farsad, H. B. Yilmaz, A. W. Eckford, C. Chae, and W. Guo, “A comprehensive survey of recent advancements in molecular communication,” *IEEE Commun. Surv. Tutorials*, vol. 18, no. 3, pp. 1887–1919, thirdquarter 2016.
- [4] W. Guo, T. Asyhari, N. Farsad, H. B. Yilmaz, B. Li, A. W. Eckford, and C. Chae, “Molecular communications: Channel model and physical layer techniques,” *IEEE Wireless Commun.*, vol. 23, no. 4, pp. 120–127, Aug. 2016.
- [5] W. Haselmayr, A. Springer, G. Fischer, C. Alexiou, H. Boche, P.A. Hoher, F. Dressler, and R. Schober, “Integration of molecular communications into future generation wireless networks,” in *Proc. IEEE 6G Wireless Summit*, Levi, Finland, Mar. 2019, pp. 1–2.
- [6] M. K. Hojo, K. Ishii, M. Sakura, K. Yamaguchi, S. Shigenobu, and M. Ozaki, “Antennal RNA-sequencing analysis reveals evolutionary aspects of chemosensory proteins in the carpenter ant, camponotus japonicus” *Scientific Reports*, vol. 5, p. 13541, Aug. 2015.
- [7] T. Suda, M. Moore, T. Nakano, R. Egashira, A. Enomoto, S. Hiyama, and Y. Moritani, “Exploratory research on molecular communication between nanomachines,” in *Proc. Genet. Evol. Comput. Conf. (GECCO)*, Washington, DC, USA, Jun. 2005, pp. 1–5.
- [8] I. Habibi, E. S. Emamian, and A. Abdi, “Quantitative analysis of intracellular communication and signaling errors in signaling networks,” *BMC Syst. Biol.*, vol. 8, no. 1, p. 89, 2014.
- [9] Y. Chahibi, “Molecular communication for drug delivery systems: A survey,” *Nano Commun. Netw.*, vol. 11, pp. 90–102, Mar. 2017.
- [10] S. Qiu, W. Guo, S. Wang, N. Farsad, and A. Eckford, “A molecular communication link for monitoring in confined environments,” in *Proc. IEEE Int. Conf. Commun. Workshops (ICC)*, 2014, pp. 718–723.
- [11] A.E. Forooshani, S. Bashir, D.G. Michelson, and S. Noghlanian, “A survey of wireless communications and propagation modeling in underground mines,” *IEEE Commun. Surv. Tutorials*, vol. 15, no. 4, pp. 1524–1545, fourthquarter 2013.
- [12] F. Gulec, and B. Atakan, “A molecular communication perspective on airborne pathogen transmission and reception via droplets generated by coughing and sneezing,” *IEEE Trans. Mol. Biol. Multi. Scale Commun.*, vol. 7, no. 3, pp. 175–184, Sep. 2021.
- [13] M. Schurwanz, P.A. Hoeher, S. Bhattacharjee, M. Damrath, L. Stratmann, and F. Dressler, “Duality between coronavirus transmission and air-based macroscopic molecular communication,” *IEEE Trans. Mol. Biol. Multi Scale Commun.*, vol. 7, no. 3, pp. 200–208, Sep. 2021.
- [14] M. Schurwanz, P.A. Hoeher, S. Bhattacharjee, M. Damrath, L. Stratmann, and F. Dressler, “Infectious disease transmission via aerosol propagation from a molecular communication perspective: Shannon meets coronavirus,” *IEEE Comm. Mag.*, vol. 59, no. 5, pp. 40–46, May 2021.
- [15] P.A. Hoeher, M. Damrath, S. Bhattacharjee, and M. Schurwanz, “On mutual information analysis of infectious disease transmission via particle propagation,” accepted for publication in *IEEE Mol. Biol. Multi Scale Commun. Lett.*, 2021, DOI 10.1109/TMBMC.2021.3120637.
- [16] N. Farsad, W. Guo, and A. W. Eckford, “Tabletop molecular communication: Text messages through chemical signals,” *PLoS ONE*, vol. 8, no. 12, pp. 1–13, Dec. 2013.
- [17] V. Jamali, A. Ahmadzadeh, W. Wicke, A. Noel, and R. Schober, “Channel modeling for diffusive molecular communication – a tutorial review,” *Proc. IEEE*, vol. 107, no. 7, pp. 1256–1301, Jul. 2019.
- [18] S. Giannoukos, S. Taylor, and J. Smith, “Molecular communication over gas stream channels using portable mass spectrometry,” *J. Am. Soc. Mass Spectrom.*, vol. 28, no. 11, pp. 2371–2383, Jul. 2017.
- [19] M. Ozmen, E. Kennedy, J. Rose, P. Shakya, J.K. Rosenstein, and C. Rose, “High speed chemical vapor communication using photoionization detectors,” in *Proc. IEEE Global Commun. Conf. (GLOBECOM)*, Abu Dhabi, United Arab Emirates, Dec. 2018, pp. 1–6.

- [20] I. Athanayake, S. Esfahani, P. Denissenko, I. Guymer, P.J. Thomas, and W. Guo, "Experimental molecular communications in obstacle rich fluids," in *Proc. ACM Int. Conf. on Nano. Comp and Commun. (NANOCOM)*, Reykjavik, Iceland, Sep. 2018, pp. 1–6.
- [21] M. Abbaszadeh, W. Li, L. Lin, I. White, P. Denissenko, P. J. Thomas, and W. Guo, "Mutual information and noise distributions of molecular signals using laser induced fluorescence," in *Proc. IEEE Global Commun. Conf. (GLOBECOM)*, Waikoloa, HI, USA, Dec. 2019, pp. 1–2.
- [22] S. Bhattacharjee, M. Damrath, and P.A. Hoeher, "Design of macroscopic air-based molecular communication concept using fluorescein," in *Proc. ACM Int. Conf. on Nano. Comp and Commun. (NANOCOM)*, Virtual Conference, Sep. 2020, pp. 1–2.
- [23] M. Damrath, S. Bhattacharjee, and P.A. Hoeher, "Investigation of multiple fluorescent dyes in macroscopic air-based molecular communication," *IEEE Trans. Mol. Biol. Multi. Scale Commun.*, vol. 7, no. 2, pp. 78–82, Jun. 2021.
- [24] M. S. Kuran, H. B. Yilmaz, T. Tungcu, and I. F. Akyildiz, "Modulation techniques for communication via diffusion in nanonetworks," in *Proc. IEEE Int. Conf. Commun. (ICC)*, Kyoto, Japan, Jun. 2011, pp. 1–5.
- [25] H. Arjmandi, A. Gohari, M.N. Kenari, and F. Bateni, "Diffusion-based nanonetorking: A new modulation technique and performance analysis," *IEEE Commun. Lett.*, vol. 17, no. 4, pp. 645–648, Apr. 2013.
- [26] D.T. McGuiness, S. Giannoukos, S. Taylor, and A. Marshall, "Analysis of multi-chemical transmission in the macro-scale," *IEEE Trans. Mol. Biol. Multi Scale Commun.*, vol. 6, no. 2, pp. 93–105, Nov. 2020.
- [27] M.C. Gursoy, E. Basar, A.E. Pusane, and T. Tugcu, "Index modulation for molecular communication via diffusion systems," *IEEE Trans. Commun.*, vol. 67, no. 5, pp. 3337–3350, May 2019.
- [28] Y. Huang, M. Wen, L. L. Yang, C. B. Chae, and F. Ji, "Spatial modulation for molecular communication," *IEEE Trans. NanoBiosci.*, vol. 18, no. 3, pp. 381–395, Jul. 2019.
- [29] Y. Huang, M. Wen, L. L. Yang, C. B. Chae, X. Chen, and Y. Tang, "Space shift keying for molecular communication: Theory and experiment," in *Proc. Global Commun. Conf. (GLOBECOM)*, Waikoloa, HI, USA, Dec. 2019, pp. 1–6.
- [30] F. Bronner and F. Dressler, "Towards mastering complex particle movement and tracking in molecular communication simulation," in *Proc. ACM Int. Conf. on Nano. Comp and Commun. (NANOCOM)*, Dublin, Ireland, Sep. 2020, pp. 1–2.
- [31] L. Felicetti, M. Femminella, G. Reali, P. Gresele, and M. Malvestiti, "Simulating an in vitro experiment on nanoscale communications by using BiNS2," *Nano Commun. Netw.*, vol. 4, pp. 172–180, Dec. 2013.
- [32] A. Noel, K.C. Cheung, R. Schober, D. Makrakis, and A. Hafid, "Simulating with AcCoRD: Actor-based communication via reaction-diffusion," *Nano Commun. Netw.*, vol. 11, pp. 44–75, Mar. 2017.
- [33] Y. Jian, B. Krishnaswamy, C. M. Austin, A.O. Bicen, J. E. Perdomo, S.C. Patel, I.F. Akyildiz, C.R. Forest, and R. Sivakumar, "NanoNS3: Simulating bacterial molecular communication based nanonetworks in network simulator 3," in *Proc. ACM Int. Conf. on Nano. Comp and Commun. (NANOCOM)*, New York, NY, USA, Sep. 2016, pp. 1–7.
- [34] M.M. Sidahmed, M.D. Taher, and R.B. Brown, "A virtual nozzle for simulation of spray generation and droplet transport" *Biosys. Eng.*, vol. 92, pp. 295–307, Nov. 2005.
- [35] J.P. Drees, L. Stratmann, F. Bronner, M. Bartunik, J. Kirchner, H. Unterweger, F. Dressler, "Efficient simulation of macroscopic molecular communication: The Pogona simulator," in *Proc. ACM Int. Conf. on Nano. Comp and Commun. (NANOCOM)*, Virtual Conference, Sep. 2020.
- [36] S. Bhattacharjee, M. Damrath, F. Bronner, L. Stratmann, J.P. Drees, F. Dressler, and P.A. Hoeher, "A testbed and simulation framework for air-based molecular communication testbed using fluorescein," in *Proc. ACM Int. Conf. on Nano. Comp and Commun. (NANOCOM)*, Virtual Conference, Sep. 2020, pp. 1–6.
- [37] M. Müller, D. Charypar, and M. Gross, "Particle-based fluid simulation for interactive applications," in *ACM SIGGRAPH/Eurographics Symp. on Comp. Ani. (SCA)*, San Diego, CA, USA, Jul. 2003, pp. 154–159.
- [38] P. Sarathi, R. Gurka, G.A. Kopp, and P.J. Sullivan, "A calibration scheme for quantitative concentration measurements using simultaneous PIV and PLIF," *Exp. in Fluids*, vol. 52, no. 1, pp. 247–259, Jan. 2012.
- [39] F. Gulec and B. Atakan, "A droplet-based signal reconstruction approach to channel modeling in molecular communication," *IEEE Trans. Mol. Biol. Multi-Scale Commun.*, vol. 7, no. 1, pp. 64–68, Mar. 2021.
- [40] N.-R. Kim, N. Farsad, C.-B. Chae, and A.W. Eckford, "A universal channel model for molecular communication systems with metal-oxide detectors," in *Proc. IEEE Int. Conf. Commun. (ICC)*, London, UK, Jun. 2015, pp. 1054–1059.
- [41] F. Gulec and B. Atakan, "Distance estimation methods for a practical macroscale molecular communication system," *Nano Commun. Netw.*, vol. 24, May 2020, Art. no. 100300.
- [42] E. A. Bucher, R. M. Lerner, and C. W. Niessen, "Some experiments on the propagation of light pulses through clouds," *Proc. IEEE*, vol. 58, no. 10, pp. 1564–1567, Oct. 1970.
- [43] R.M. Gagliardi and S. Karp, *Optical Communication*. New York, NY: Wiley, 2nd ed., 1995.
- [44] M. Damrath, S. Korte, and P.A. Hoeher, "Equivalent discrete-time channel modeling for molecular communication with emphasize on an absorbing receiver," *IEEE Trans. NanoBiosci.*, vol. 16, no. 1, pp. 60–68, Jan. 2017.
- [45] D. S. Shiu and J. M. Kahn, "Differential pulse-position modulation for power-efficient optical communication," *IEEE Trans. on Commun.*, vol. 47, no. 8, pp. 1201–1210, Aug. 1999.
- [46] M. Sui and Z. Zhou, "The modified PPM modulation for underwater wireless optical communication," in *Proc. IEEE Int. Conf. on Comm. Soft. and Netw.*, Macau, China, Feb. 2009, pp. 173–177.
- [47] H. Sugiyama and K. Nosu, "MPPM: A method for improving the band-utilization efficiency in optical PPM," *J. Lightwave Tech.*, vol. 7, no. 3, pp. 465–472, Mar. 1989.
- [48] B. Koo, C. Lee, H. B. Yilmaz, N. Farsad, A. Eckford and C. Chae, "Molecular MIMO: From Theory to Prototype," *IEEE J. Sel. Areas Commun.*, vol. 34, no. 3, pp. 600–614, Mar. 2016.
- [49] M. U. Mahfuz, D. Makrasis, and H.T. Mouftah, "On the detection of binary concentration-encoded unicast molecular communication in nanonetworks," in *Proc. Int. Conf. on Bio-Inspired Syst. Signal Process. (BIOSIGNALS)*, Rome, Italy, Jan. 2011, pp. 26–29.
- [50] M. Damrath and P. A. Hoeher, "Low-complexity adaptive threshold detection for molecular communication," *IEEE Trans. NanoBiosci.*, vol. 15, no. 3, pp. 200–208, Apr. 2016.
- [51] J.G. Proakis and M. Salehi, *Digital Communications*. New York: McGraw-Hill, 5th ed., 2007.
- [52] G. D. Forney, "The Viterbi algorithm," *Proc. IEEE*, vol. 61, no. 3, pp. 268–278, Mar. 1973.